Controllable growth of Prussian blue nanostructures on carboxylic group-functionalized carbon nanofibers and its application for glucose biosensing

2012 Nanotechnology 23 455502

(http://iopscience.iop.org/0957-4484/23/45/455502)

Nanotechnology **23** (2012) 455502 (10pp) doi:10.1088/0957-4484/23/45/455502

Controllable growth of Prussian blue nanostructures on carboxylic group-functionalized carbon nanofibers and its application for glucose biosensing

Li Wang, Yinjian Ye, Haozhi Zhu, Yonghai Song, Shuijian He, Fugang Xu and Haoqing Hou

College of Chemistry and Chemical Engineering, Jiangxi Normal University, 99 Ziyang Road, Nanchang 330022, People's Republic of China

E-mail: lwangsy2003@hotmail.com and hqhou@jxnu.edu.cn

Received 3 May 2012, in final form 21 August 2012
Published 22 October 2012
Online at stacks.iop.org/Nano/23/455502

Abstract

Glucose detection is very important in biological analysis, clinical diagnosis and the food industry, and especially for the routine monitoring of diabetes. This work presents an electrochemical approach to the detection of glucose based on Prussian blue (PB) nanostructures/carboxylic group-functionalized carbon nanofiber (FCNF) nanocomposites. The hybrid nanocomposites were constructed by growing PB onto the FCNFs. The obtained PB–FCNF nanocomposites were characterized by scanning electron microscopy, x-ray diffraction and x-ray photoelectron spectroscopy. The mechanism of formation of PB–FCNF nanocomposites was investigated and is discussed in detail. The PB–FCNF modified glassy carbon electrode (PB–FCNF/GCE) shows good electrocatalysis toward the reduction of H_2O_2, a product from the reduction of O_2 followed by glucose oxidase (GOD) catalysis of the oxidation of glucose to gluconic acid. Further immobilizing GOD on the PB–FCNF/GCE, an amperometric glucose biosensor was achieved by monitoring the generated H_2O_2 under a relatively negative potential. The resulting glucose biosensor exhibited a rapid response of 5 s, a low detection limit of 0.5 μM, a wide linear range of 0.02–12 mM, a high sensitivity of 35.94 μA cm^{-2} mM^{-1}, as well as good stability, repeatability and selectivity. The sensor might be promising for practical application.

(Some figures may appear in colour only in the online journal)

1. Introduction

Glucose, as an essential physiological component, is distributed extensively in the blood of organisms and in foods and pharmaceuticals [1]. It is often used as a marker of diabetes which has become one of the major diseases worldwide [2]. Therefore, the quantitative determination of glucose level not only in blood but also in other sources such as foods and pharmaceuticals is very important in biological and clinical analysis [3–6].

To date, various techniques have been developed for glucose determination, including electrochemistry [7], capillary zone electrophoresis [8], Fourier transform infrared spectroscopy [9], fluorescence spectroscopy [10–13], surface plasmon resonance [14], etc. Among those techniques, electrochemistry has attracted significant attention because of its high sensitivity, low cost, simplicity and rapid response [15, 16]. The electrochemical approach for glucose detection can be realized by using glucose oxidase (GOD) as the recognition element to monitor the current change during the process of oxidation of glucose catalyzed by GOD [17]. Trace glucose could also be determined by using nanomaterials as a catalyst to electrochemically oxide

glucose. Many nanomaterials, including CuO [18], Cu [19, 20], MnO_2 [21], NiO_2 [22], Ni [23], etc, have been widely used to construct electrochemical glucose sensors. The determination of glucose is based on the direct oxidation of glucose. However, the oxidation of glucose catalyzed by nanomaterials usually requires a relatively high positive potential. Many other species coexisting in biological fluids can also be oxidized under such a high potential, thus their electrochemical signals may severely affect the selectivity of the assay.

A method to overcome the interference is to monitor the generated H_2O_2 at a relatively negative potential, since GOD catalyzes the oxidation of glucose to gluconic acid, followed by production of H_2O_2 [24, 25]. Thus, quantification of glucose can be achieved by measuring the amount of enzymatically generated H_2O_2. Prussian blue (PB) [26], as a prototype metal hexacyanoferrate with a formula of $Fe_4^{III}[Fe^{II}(CN)_6]_3$, has been widely used as the electron-transfer mediator in electrochemical H_2O_2 sensors because it can catalyze the electrochemical reduction of H_2O_2 at low potentials (it is usually referred to as artificial peroxidase) [27–30]. Carbon nanofibers (CNFs) have recently attracted considerable attention for their large surface area and good conductivity [31–34]. Electrochemical investigations have shown that CNFs are capable of promoting electron transfer, minimizing electrode surface fouling and enhancing electrocatalytic activity [31–34]. CNFs decorated with metal nanoparticles (NPs), including PtNPs [32], NiNPs [33], CoNPs [34] and Pt/AuNPs [35], could be used as electrode materials to construct a sensor.

In this work, PB–carboxylic group-functionalized carbon nanofiber (FCNF) nanocomposites were constructed by controllable growth of PB nanostructures on FCNFs. The PB–FCNF nanocomposites show good stability in neutral solution and their formation mechanism is discussed. A novel glucose biosensor was developed by immobilizing GOD on a PB–FCNF nanocomposite modified glassy carbon electrode (GCE). The experimental conditions related to the preparation of PB–FCNF nanocomposites and the performances of the resulted biosensors were investigated in detail.

2. Experimental details

2.1. Reagents and materials

Chitosan (CS; 75% deacetylation), GOD (EC1.1.3.4, Type X-S, lyophilized powder, 117 U mg^{-1}, from *Aspergillus niger*), D-(+)-glucose (≥99.5%), polyacrylonitrile (PAN; MW 269,000 g mol^{-1}) and *N*,*N*-dimethylformamide (DMF) were purchased from Sigma-Aldrich (St Louis, USA). Cetyl trimethyl ammonium bromide (CTAB; $CH_3(CH_2)_{15}N(CH_3)_3Br$) was obtained from Tianjin Yongda Chemical Reagents Development Company (Tianjin, China). Other chemicals and materials [such as ferric (III) chloride, potassium ferricyanide, potassium chloride, acetic acid, hydrogen peroxide (H_2O_2, 30%), etc] were obtained commercially from the Beijing Chemical Reagent Factory (Beijing, China). All reagents were of analytical grade and used as-received without further purification. Phosphate buffer solutions (PBS; 0.05 M, pH 7.0) were prepared with KH_2PO_4 and K_2HPO_4, containing 0.1 M KCl. GOD solution (200 μM) was made in 0.05 M PBS (pH 7.0). All solutions were prepared with ultra-pure water purified by a Millipore-Q System (18.2 MΩ cm).

2.2. Preparation of CNFs and FCNFs

CNFs were prepared by first electrospinning of PAN to obtain PAN nanofibers, followed by carbonization of these nanofibers at high temperature [36]. Briefly, PAN was dissolved in DMF. Then CTAB (0.2 wt%) and acetone (5 wt%) were added into the mixed solution to reduce the surface tension and increase the conductivity of the solution. The as-prepared homogeneous solution was electrospun by applying an electrical potential of 30 kV at a distance of 30 cm between the spinneret and the collector. In an electrical field of the order of 100 kV m^{-1}, the PAN nanofibers were formed. Stabilization and carbonization of PAN nanofibers was completed in a high-temperature furnace by the following steps: (1) 230 °C annealing in air for 3 h to partially oxidize the PAN; (2) heating up to 300 °C at a rate of 5 °C min^{-1} and staying at this temperature in a H_2 and Ar mixture ($H_2/Ar = 1/3$) for 2 h for shape stabilization of the nanofibers; (3) heating up to 1200 °C in Ar at a rate of 5 °C min^{-1} to carbonize the nanofibers, staying at this temperature for 0.5 h, and then cooling down to room temperature in Ar.

FCNFs were prepared according to our reported method [31]. Briefly, CNFs of a certain mass were boiled in 65% nitric acid for 12 h. After centrifugation from the mixture, the sediment was washed with ultra-pure water until the pH reached 7.0. Then the product was dried at 100 °C in an oven to obtain FCNFs.

2.3. Synthesis of PB–FCNF nanocomposites

The PB–FCNF nanocomposites were prepared according to a previous procedure [32]. Briefly, 10 mg of FCNFs was reacted with 10 ml of $FeCl_3$ aqueous solution (1.0 mM) by ultrasonic agitation for 1 h. Then 10 ml of 1 mM aqueous solution of $K_3Fe(CN)_6$ was added dropwise to this mixture with continuous stirring at room temperature. After that, the mixture was maintained at ambient conditions for different reaction times to yield a suspension of PB–FCNF nanocomposites. The solid product was then centrifuged and washed with ultra-pure water several times until Cl^- could not appear by reacting with $AgNO_3$. Finally, the product was dried at 50 °C for 24 h in an oven.

2.4. Preparation of a PB–FCNF/GCE

A GCE (3 mm in diameter) was polished on a polishing cloth with 1.0, 0.3, 0.05 μm alumina powder, respectively. Then the polished GCE was rinsed with ultra-pure water followed by sonicating in ultra-pure water for 1 min. A defined quantity of PB–FCNFs (about 1 mg) was suspended in 200 μl ultra-pure water containing 5 μl CS (0.5 wt%) and sonicated for 30 min. Then a drop of the suspension (10 μl) was cast on the polished

GCE surface and dried in an inverted beaker in air. When the resultant PB–FCNF/GCE was not in use, it was stored in the inverted beaker at room temperature.

2.5. Fabrication of the GOD/PB–FCNF/GCE modified electrode

GOD (5.0 μl) and CS (3.0 μl) solutions (0.5 wt%) were mixed and dropped onto the PB–FCNF/GCE, followed by drying in air for 12 h to obtain a GOD/PB–FCNF/GCE. When the GOD/PB–FCNF/GCE was not in use it was also stored in the inverted beaker at 4 °C.

2.6. Apparatus

All electrochemical experiments were performed by a CHI 660C electrochemical workstation (CH Instruments, Shanghai, China) using a conventional three-electrode system with a bare or modified GCE as the working electrode, a platinum wire as the auxiliary electrode, and Ag/AgCl (saturated KCl) as the reference electrode. The cyclic voltammetric (CV) experiments were performed in a quiescent solution. The amperometric experiments were carried out in a continuously stirred solution using a magnetic stirrer. X-ray powder diffraction (XRD) data were collected on a D/Max 2500 V/PC x-ray powder diffractometer using Cu Kα radiation ($\lambda = 1.540\,56$ Å, 40 kV, 200 mA). The scanning electron microscopy (SEM) analysis was taken using a XL30 ESEM-FEG SEM at an accelerating voltage of 20 kV equipped with a Phoenix energy dispersive x-ray analyzer (EDXA). X-ray photoelectron spectroscopy (XPS) measurement was performed on an ESCALAB-MKII spectrometer (VG Co., UK) with Al Kα x-ray radiation as the x-ray source for excitation.

3. Results and discussion

3.1. Controllable growth of PB–FCNF nanocomposites

To fabricate PB–FCNF nanocomposites, CNFs were first oxidized into FCNFs with nitric acid to provide some carboxyl groups [31]. After the FCNFs were immersed into a solution of Fe^{3+}, the Fe^{3+} strongly interacted with carboxyl groups and adsorbed on the carboxyl groups based on the electrostatic interactions and coordination interaction [27]. Then the $Fe(CN)_6^{3-}$ would coordinate with the Fe^{3+} on the surface of FCNFs, resulting in the formation of a Fe^{III}–$Fe^{III}(CN)_6^{3-}$ complex after $Fe(CN)_6^{3-}$ was added [29]. Previous reports have demonstrated that PB nanomaterials could be prepared by directly mixing Fe^{3+} and $Fe(CN)_6^{3-}$ in the presence of reducing agents such as single-walled carbon nanotubes (SWNTs) [29, 30] and graphene [27, 28]. The spontaneous formation of PB–SWNTs was ascribed to the different reduction potential between SWNTs and the Fe^{III}–$Fe^{III}(CN)_6^{3-}$ complex [29]. The Fe^{III}–$Fe^{III}(CN)_6^{3-}$ complex has a high open circuit potential (about +1.22 V versus standard hydrogen electrode, SHE) in acidic media and accordingly is a very strong oxidant. The Fermi level of the SWNTs is approximately +0.5 V versus SHE [29]. Therefore, electrons could spontaneously transfer from the SWNTs to the Fe^{III}–$Fe^{III}(CN)_6^{3-}$ complex and the Fe^{III}–$Fe^{III}(CN)_6^{3-}$ complex would be reduced to Fe^{III}–$Fe^{II}(CN)_6^{4-}$ [29]. Similar to that, in the presence of a reducing agent of FCNFs, the electron transfer from FCNFs to the absorbed Fe^{III}–$Fe^{III}(CN)_6^{3-}$ might result in the formation of PB nanostructures. Compared to PB nanomaterials synthesized by directly mixing Fe^{3+} and $Fe(CN)_6^{4-}$, the morphology and size of the PB nanostructures obtained in this work could be well controlled by adjusting the reaction time. The formation mechanism of the PB–FCNF nanocomposites was confirmed by SEM (figure 1). The SEM image of bulk CNFs (figure 1(A)) shows a uniform surface topography with cross and three-dimensional structure. The CNFs have a diameter of about 300 nm and are tens of micrometers in length. After they were treated in nitric acid for 12 h, the original construction of CNFs was well maintained (figure 1(B)). After the FCNFs were immersed into the mixed solution of Fe^{3+} and $Fe(CN)_6^{3-}$ for 144 h, it was evident that a large number of PB nanostructures were randomly deposited on the surface of the FCNFs (figure 1(D)). The large-scale SEM image showed the PB–FCNF nanocomposites had a homogeneous structure: nanorods and nanosheets. Moreover, the obtained PB–FCNF nanocomposites could be well dispersed in water and ethanol for further application. However, on the bare glassy carbon substrate, there were only big and aggregated PB NPs covering the surface, forming a compact film (figure 1(C)). The results indicated that the three-dimensional FCNFs might play a crucial role in the morphology and size of PB nanostructures.

The growth process of PB–FCNF nanocomposites as a function of reaction time was followed by SEM (figure 2). In the first 3 h, only a few PB NPs formed and deposited on the FCNF surface (figure 2(A)). As the reaction time increased to 12 h, many PB NPs were produced and aggregated (figure 2(B)). After 96 h, some PB NPs began to inosculate into nanorods and nanosheets as shown in figure 2(C). A large number of nanorods and nanosheets were produced and formed a porous film when the reaction time was increased to 144 h (figure 2(D)). The results suggested that the growth of PB–FCNF nanocomposites was controllable by changing the reaction time.

XPS analysis provides detailed information on the chemical composition of the as-prepared PB–FCNF nanocomposites. The fully scanned spectra of FCNFs demonstrated that only C and O elements existed in FCNFs (curve (a) in figure 3(A)) [31]. Whereas after the FCNFs interacted with Fe^{3+} and $Fe(CN)_6^{3-}$, the XPS spectrum indicated the presence of N and Fe elements in the PB–FCNF nanocomposites (curve (b) in figure 3(A)). To further understand the electronic states of the elements, more attention was paid to the high-resolution spectra of Fe and N. The binding energies at 711.3 and 724.8 eV were assigned to Fe^{3+} in $Fe_4^{III}[Fe^{II}(CN)_6]_3$ (inset (a) in figure 3(A)) [37]. The energy at 708.3 eV could be assigned to Fe^{2+} of $Fe_4^{III}[Fe^{II}(CN)_6]_3$ (inset (a) in figure 3(A)) [37]. The main peak of the N core-level spectra was fitted with three components at 401.7, 399.5 and 397.4 eV (inset (b) in

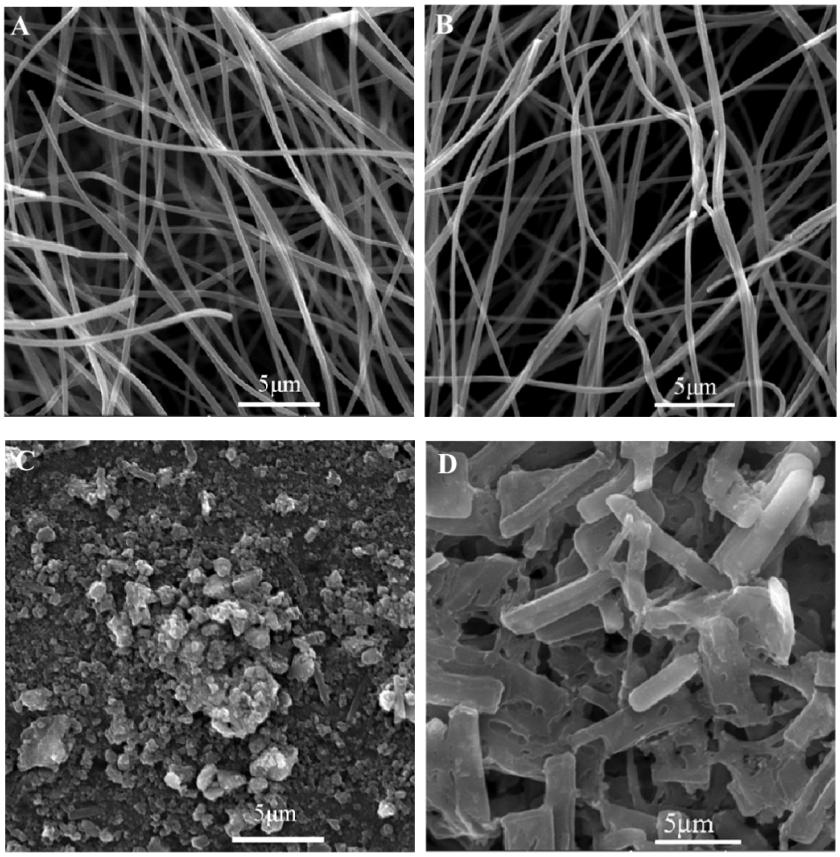

Figure 1. SEM images of CNFs (A), FCNFs (B), PB (C) and PB–FCNF nanocomposites (D).

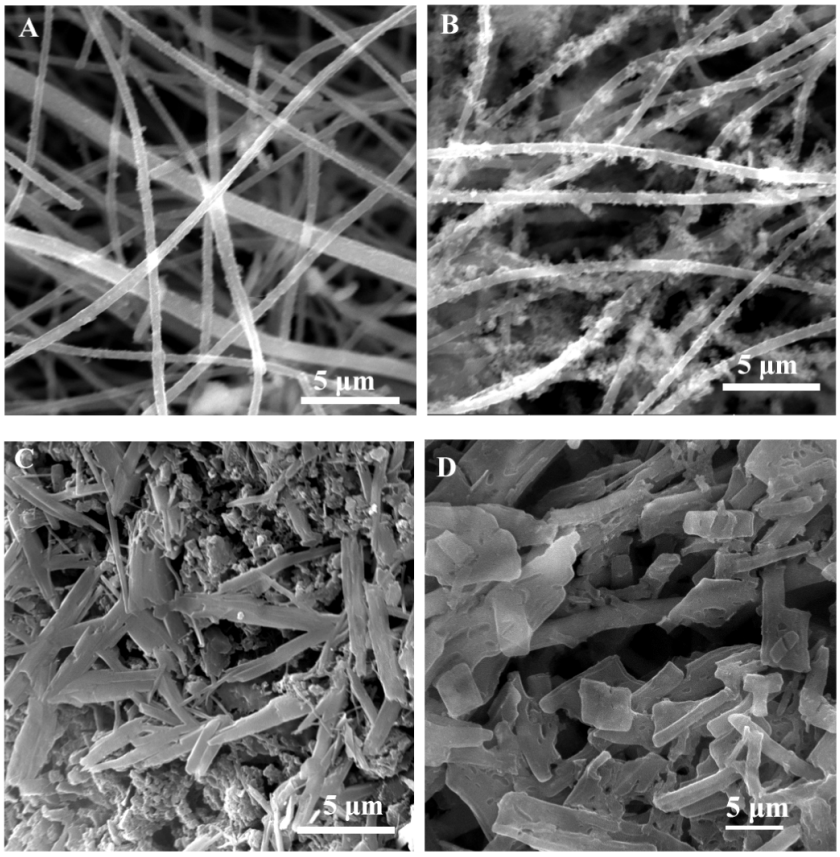

Figure 2. SEM images of PB–FCNF nanocomposites obtained at different reaction times: 3 h (A), 12 h (B), 96 h (C) and 144 h (D).

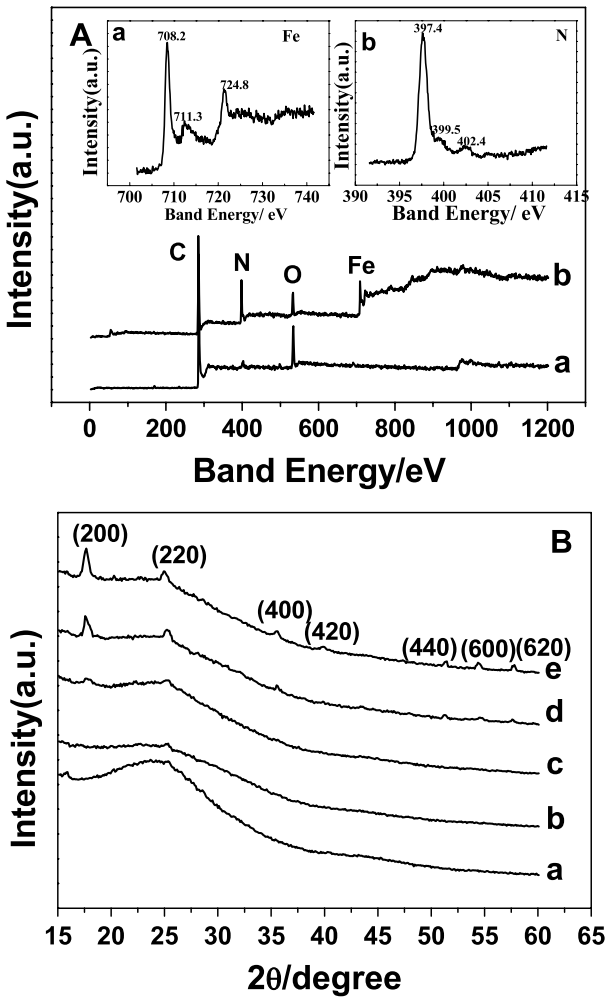

Figure 3. XPS spectra (A) and XRD pattern (B) of FCNFs (curve (a)) and PB–FCNF nanocomposites ((b)–(e)) obtained at different reaction times: 3 h (b), 12 h (c), 96 h (d) and 144 h (e). Insets a and b in figure 2(A) show the XPS spectra of Fe and N, respectively.

figure 3(A)), respectively, indicating the existence of C–N ($Fe_4^{III}[Fe^{II}(CN)_6]_3$) in the PB–FCNF nanocomposites [37]. On the basis of the high-resolution spectra of N and Fe, we could conclude that PB nanocrystals were successfully synthesized on FCNF surface.

The formation of PB–FCNF nanocomposites was further identified by XRD (figure 3(B)). The diffraction peaks close to 26° can be assigned to the diffraction of (002) planes of the FCNFs (JCPDS card number 13-0148) (curve (a) in figure 3(B)), which indicated that the graphitic structure of FCNFs was formed as a consequence of the heat treatment [31]. Peaks located at 17.6, 24.8, 35.3, 39.6, 43.6, 50.7, 54.2 and 57.2° can be indexed to the (200), (220), (400), (420), (422), (440), (600) and (620) planes of a pure face-centered-cubic $Fe_4^{III}[Fe^{II}(CN)_6]_3$ (JCPDS card number 73-0687), respectively (curve (e) in figure 3(B)) [37]. The result demonstrates the successful synthesis of PB–FCNF nanocomposites. The XRD spectra of PB–FCNF nanocomposites obtained with different reaction times were also investigated (figure 3(B)). There were no obvious diffraction peaks for the nanocomposites prepared with a 3 and 12 h reaction time (curves (b) and (c) in figure 3(B)). As the reaction time increased, the peaks indexed to the planes of PB appeared and enhanced (curves (d) and (e) in figure 3(B)). The XRD result further demonstrates the successful synthesis of PB–FCNF nanocomposites.

According to the obtained results, a reasonable route was used to explain the growth mechanism of the PB nanostructures. After FCNFs were immersed into a solution containing Fe^{3+}, Fe^{3+} was absorbed onto the carboxyl groups of the FCNFs based on the electrostatic interactions and coordination interaction between Fe^{3+} and carboxyl groups [27]. $Fe(CN)_6^{3-}$ would coordinate with Fe^{3+} on the surface of the FCNFs, resulting in the formation of a Fe^{III}–$Fe^{III}(CN)_6^{3-}$ complex after the $Fe(CN)_6^{3-}$ was added [29]. Electron transfer from FCNFs to the absorbed Fe^{III}–$Fe^{III}(CN)_6^{3-}$ might result in the formation of a PB nanostructure. As reported by Zhang *et al* [38], the formation of a uniform crystalline structure arises from the template-directed aggregation of small particles and subsequent recrystallization rather than simple aggregation of small particles. The newly formed PB seeds might move along the FCNFs to the nearest nucleation spot, leading to the growth of the PB NP core. This main principle was similar to the explanation for the preparation of noble metal NPs on nanoporous DNA networks films [39]—that the size of NPs could increase with the reaction time. When the reaction time was extended to 144 h, the final products grew into nanorods and nanosheets. It is obvious that the final product is controllable by the reaction time. In previous reported work, an accepted mechanism for the formation of Au nanorods on a surface is that Au deposited directly onto surface-attached AuNP seeds and formed Au nanorods [40]. In this work, there were many PB seeds formed on the FCNFs, but no PB nanorods were generated at short reaction times. It is not enough to form the PB nanorods when there are only seeds, since nanorod nucleation is thought to require twinned seed particles, and seed aggregation as a source of twinning may be an important step in nanorod synthesis. As the reaction time increased, a large number of PB NPs were generated on the FCNFs. The distance between two PB NPs became very close, some PB NPs could easily move along the FCNFs and adsorb onto the deposited NPs, and these aggregated NPs could form nanorods by subsequent recrystallization. As the reaction time was further increased, the PB nanorods gradually became large in diameter, suggesting that the Fe^{III}–$Fe^{III}(CN)_6^{3-}$ complex in a solution could be slowly reduced into PB NPs. The formed PB NPs slowly deposited on the PB nanorods and resulted in the distance between two PB nanorods becoming very close. Finally, nanosheets would be formed on the FCNFs. In the absence of FCNFs, no nanorods or nanosheets were found, also supporting the proposed mechanism.

3.2. Electrochemical behavior of the PB–FCNF/GCE

The electrochemical behavior of the PB–FCNF/GCE was investigated by CV experiments. Figure 4(A) shows the CVs of different modified electrodes in 0.05 M PBS + 0.1 M KCl (pH 6.0). The CV response of pure FCNFs and PB modified

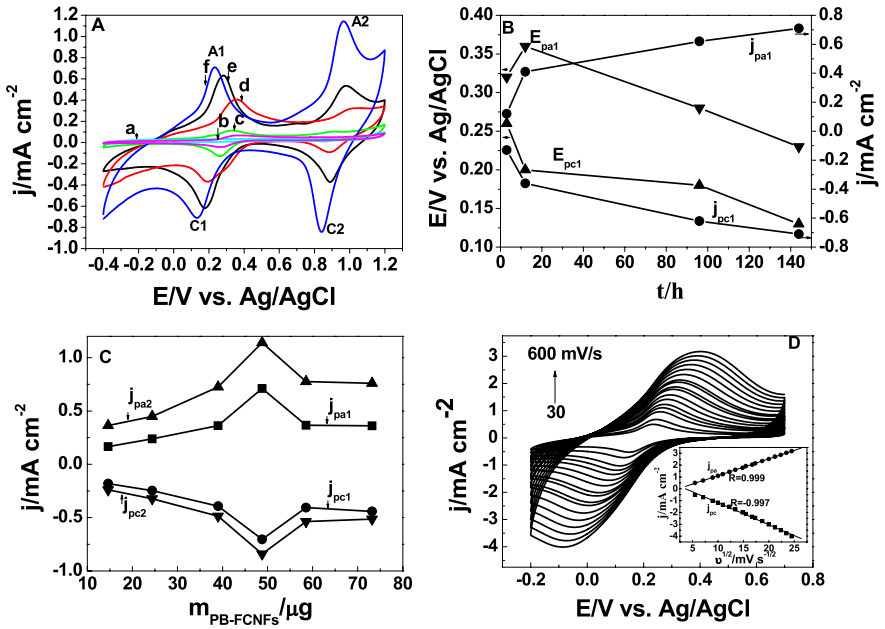

Figure 4. (A) CVs of GCEs modified with FCNFs (a), PB (b) and PB–FCNF nanocomposites obtained at different reaction times: 3 (c), 12 (d), 96 (e) and 144 h (f). Supporting electrolyte 0.05 M PBS + 0.1 M KCl (pH 6.0); scan rate 50 mV s^{-1}. (B) Plots of peak current (j_{p1}) and peak potential (E_{p1}) versus the reaction time. (C) Plots of peak current density versus the quantity of PB–FCNFs. (D) CVs of the PB–FCNF/GCE in 0.05 M PBS + 0.1 M KCl (pH 6.0) at various scan rates. Inset: the plot of peak current density versus square root of scan rates.

GCEs (FCNF/GCE and PB/GCE) are displayed as curves (a) and (b), respectively, in figure 4(A). Obviously no peak current was observed at the FCNF/GCE and only a small current appeared at the PB/GCE. After PB was deposited onto FCNFs, the peak current increased significantly and further increased as the reaction time increased (curves (c)–(f) in figure 4(A)). The results suggested that FCNFs did provide a large surface area to produce a large number of PB nanostructures. Taking the PB–FCNF/GCE acquired at 144 h as an example (curve (f) in figure 4(A)), there were two anodic peaks at 0.23 V (A_1) and 0.97 V (A_2), respectively. On the reverse scan, the corresponding cathodic peaks C_1 and C_2 appeared at 0.13 and 0.84 V, respectively. The corresponding $E_{1/2}$ for the two redox transitions A_1/C_1 and A_2/C_2 are 180 and 905 mV, respectively. When the freshly deposited $Fe_4^{III}[Fe^{II}(CN)_6]_3$ were cycled in a solution containing K^+ in a potential of −0.4–1.2 V, $Fe_4^{III}[Fe^{II}(CN)_6]_3$ was transformed to $KFe^{III}[Fe^{II}(CN)_6]$ [26]. The $Fe_4^{III}[Fe^{II}(CN)_6]_3$ lost one quarter of the high spin iron Fe^{3+}, and the K^+ occupied interstitial sites in the structure of $KFe^{III}[Fe^{II}(CN)_6]$ [26]. According to previous results [24, 25], the first redox (A_1/C_1) was ascribed to the transitions of new PB ($KFe^{III}[Fe^{II}(CN)_6]$) and Prussian white (PW; $K_2Fe^{II}[Fe^{II}(CN)_6]$) and the second redox ($A_2/C_2$) was attributed to the transitions of new PB and Berlin green (BG; $Fe^{III}[Fe^{III}(CN)_6]$). The two couples of redox peaks in the CVs might be represented by the following reactions [24]:

$$\text{Peak } (A_1/C_1) \qquad K_2Fe^{II}[Fe^{II}(CN)_6] \Leftrightarrow KFe^{III}[Fe^{II}(CN)_6] + K^+ + e \quad (1)$$

$$\text{Peak } (A_2/C_2) \qquad KFe^{III}[Fe^{II}(CN)_6] \Leftrightarrow Fe^{III}[Fe^{III}(CN)_6] + K^+ + e. \quad (2)$$

Generally, the A_1/C_1 peak was obviously larger than the A_2/C_2 peak at the PB NP modified electrode [24, 25]. However, the A_2/C_2 peak was obviously larger than the A_1/C_1 peak here. The result was consistent with previous results for a PB nanocube/SWNT modified electrode [29], indicating that the nanostructure of crystalline PB also might play an important role in the redox of PB–FCNF nanocomposites. Figure 4(B) shows the plots of peak current density (j_{p1}) and peak potential (E_{p1}) versus the reaction time. As the reaction time increased, the PB nanostructures increased and aggregated gradually, and accordingly the redox peak increased (curves c–f in figure 4(A)) as shown in figure 4(B). After 144 h, the redox peak current reached the maximum value (curve e in figure 4(A)). The peak potential gradually shifted negatively.

The effect of the quantity of PB–FCNF nanocomposites of the prepared PB–FCNF/GCE on the peak current density was also investigated (figure 4(C)). The current response increased with the increase in the quantity of PB–FCNF nanocomposites, and reached a maximum value at 50 μg. After that, the current density decreased gradually as the quantity of PB–FCNF nanocomposites further increased and stopped at 60 μg. This phenomenon might be ascribed to the following two factors. On the one hand, the small quantity of PB–FCNF nanocomposites resulted in fewer PB–FCNFs assembled on the electrode surface to form porous PB–FCNF film. The porous structure of PB–FCNF film was helpful for electron and mass transfer. On the other hand, the large number of PB–FCNF nanocomposites on the surface of the electrode might produce a compact PB–FCNF film on the electrode surface to hinder electron and mass transfer. Only the outermost layer of PB–FCNFs could take part in the

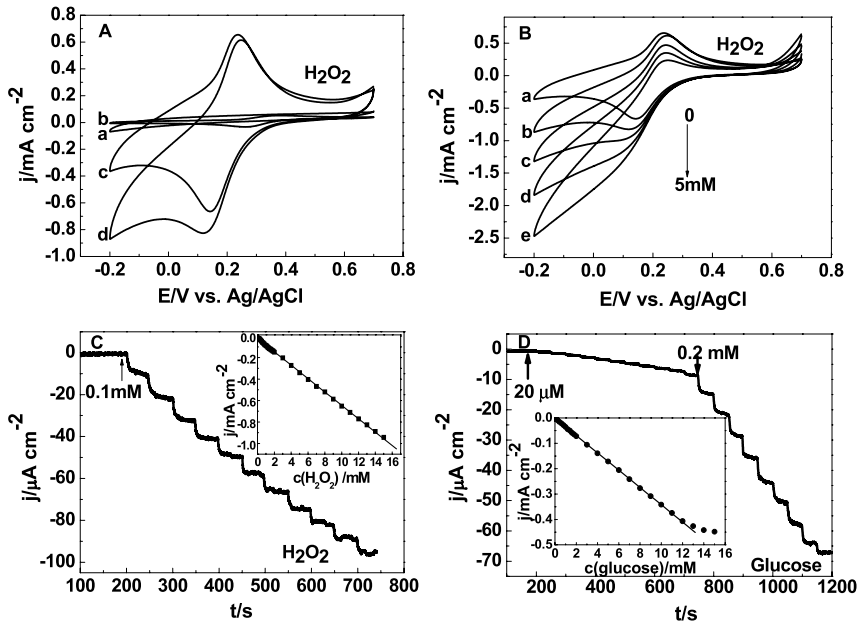

Figure 5. (A) CVs of various electrodes in 0.05 M PBS + 0.1 M KCl (pH 6.0) in the presence (a, b, d) and absence (c) of 1.0 mM H_2O_2: FCNF/GCE (a), PB/GCE (b), PB–FCNF/GCE (c, d). (B) CVs of a PB–FCNF/GCE in 0.05 M PBS + 0.1 M KCl (pH 6.0) in the presence of H_2O_2 with different concentrations at a scan rate of 50 mV s^{-1}: 0 (a), 1 (b), 2 (c), 3 (d), 4 (e) and 5 (f) mM. (C) Typical steady-state response to successive addition of H_2O_2 in 0.05 M PBS + 0.1 M KCl (pH 6.0) at a PB–FCNF/GCE. Inset: the plot of the corresponding calibration curve. Applied potential: 0.12 V. (D) Typical steady-state response to successive addition of glucose in 0.05 M PBS + 0.1 M KCl (pH 6.0) at a GOD/PB–CNF/GCE. Inset: the plot of the calibration curve. Applied potential: 0.12 V.

redox reaction, and accordingly the current density was kept constant.

To further understand the electrochemical behaviors of the PB–FCNF/GCE electrode, we paid more attention to the redox transitions A_1/C_1. Figure 4(D) shows the CVs of the PB–FCNF/GCE in 0.05 M PBS + 0.1 M KCl for a scan rate ranging from 30 to 600 mV s^{-1}. In the potential range of −0.2–0.7 V, the peak current density grew as the scan rate increased. The peak current density was proportional to the square root of scan rate, as shown by the inset in figure 4(D), indicating that the electron-transfer reaction involved a diffusion-controlled process. As mentioned above, the redox process of PB–FCNF nanocomposites was accompanied by the transfer of K^+. Thus, the slow diffusion of K^+ might control the electrochemical process and result in the linear dependence of the peak current density on the square root of scan rate.

3.3. Electrocatalytic reduction of H_2O_2 on the PB–FCNF/GCE

The sensing application of the PB–FCNF/GCE was investigated. Figure 5(A) shows the CVs of different electrodes in 0.05 M PBS + 0.1 M KCl in the presence (curves a, b, d) and absence (curve c) of 1 mM H_2O_2. For the PB–FCNF/GCE, it was observed that the reduction peak at about 0.12 V increased greatly and the oxidation peak decreased slightly in the presence of 1.0 mM H_2O_2 (curve d) as compared to that in the absence of H_2O_2 (curve c). Obviously, the PW nanostructures catalyzed the reduction of H_2O_2 and produced a remarkable catalytic current density. This result indicates that H_2O_2 is reduced by active PW species with a cyclic mediation redox processes. The mechanism of the cyclic mediation redox process is EC' catalysis [24, 25]. In this mechanism, PB is reduced to PW first and then PW species reduced the H_2O_2 followed by the regeneration of PB. There was no obvious reduction peak at the FCNF/GCE (curve a). The reduction peak at 0.12 V at the PB/GCE (curve b) was much smaller than that at the PB–FCNF/GCE (curve d). With the increase in H_2O_2, the catalytic current density at the PB–FCNF/GCE increased gradually, as shown by curves (a)–(e) in figure 5(B), exhibiting good electrocatalytic ability for the reduction of H_2O_2. The high catalytic current density was mainly ascribed to the large number of PB–FCNF nanocomposites on the electrode, the quantum scale dimension of these PB nanostructures and the porous structure of the PB–FCNF film. The FCNFs on the electrode provided a medium to greatly increase the quantity of PB nanostructures and good conductivity. Furthermore, the good catalytic activity might also result from the synergistic effect between FCNFs and PB. Thus, these PB–FCNF nanocomposites produced more active sites on the same electrode surface in the NP-assisted catalysis.

The amperometric response of the PB–FCNF/GCE for successive addition of 0.1 mM H_2O_2 was investigated as shown in figure 5(C). The reduction current density reached a maximum steady-state value and achieved 95% of the steady-state current density within 5 s. The inset in the figure 5(C) shows the calibration curve of the sensor. The linear range of the H_2O_2 detection was from 4.2 μM to 25.0 mM ($r = 0.999$) with a slope of 62.35 μA cm^{-2} mM^{-1}.

Table 1. Comparison of the performance of various glucose sensors constructed based on PB. (Note: GE, graphite electrode; GO, graphene oxide; PEDOT, poly(3,4-ethylenedioxythiophene); MWCNTs, multi-walled carbon nanotubes; SPCP, solid paraffin carbon paste; ConA, Concanavalin A; GR, graphene; PVP, polyvinylpyrrolidone; nr, not reported. Other abbreviations as in text) .

	Detection limit (μmol l^{-1})	Linear range (mmol l^{-1})	Sensitivity (μA cm^{-2} mM^{-1})	References
GOD/Nafion/PB/GE	10	0.002–0.14	nr	[24]
GOD-CS/PB/GO/GCE	0.34	0.1–13.5	nr	[25]
GOD-CS/PB–SWNT/GCE	5	0.5–13.5	nr	[29]
GOD/PEDOT/PB/MWCNT/GCE	nr	1–10	2.67	[42]
GOD/PB/CS/Au electrode	0.3 ± 0.1	0.01–5.5	97.18	[43]
GOD/Fe_3O_4-PB/SPCP electrode	0.1	0.05–8	nr	[44]
GOD/Con A/CS-PB-GR/GCE	10	0.25–3.2	nr	[45]
GOD/PB-PVP/polyaniline/MWCNT/GCE	0.6	0.067–1.9	6.28	[46]
GOD/PB–FCNF/GCE	0.538	0.02–12	35.94	This work

The detection limit was estimated to be 0.7 μM based on the criterion of a signal-to-noise ratio of 3.

3.4. Amperometric responses of the GOD/PB–FCNF/GCE

Due to the good electrocatalytic activity of PB–FCNF nanocomposites in the reduction of H_2O_2, a PB–FCNF nanocomposite-based glucose biosensor was further developed. Since chitosan has a great number of amino groups, which can provide a suitable microenvironment for GOD, CS was chosen to immobilize GOD onto the PB–FCNF/GCE for construction of a glucose biosensor [41]. Figure 5(D) shows the amperometric response of the resultant GOD/PB–FCNF/GCE to glucose in air-saturated stirred 0.05 M PBS + 0.1 M KCl (pH 6.0). The time required to reach the 95% steady-state response was within 5 s at the biosensor. The inset in figure 5(D) shows the calibration curve of the glucose sensor. The linear range of glucose detection was from 0.02 to 12 mM ($r = 0.9998$) with a slope of 35.94 μA cm^{-2} mM^{-1}. The detection limit was estimated to be 0.5 μM based on the criterion of a signal-to-noise ratio of 3. It is well known that the diabetic glucose concentration is above 7.0 mM [41], which indicates that the resulting biosensor is suitable for the practical determination of human blood glucose concentration.

A comparison of the performance of our newly designed sensor to those already reported in literature regarding the performance of glucose assay is listed in table 1. Up to now, many sensors have been developed based on PB for the detection of glucose, and all of them have some advantages and limitations [42–46]. Taking the GOD/PB/CS/Au electrode [43] as an example, the detection limit was pretty low, while the linear range was rather narrow. Compared to those sensors, the linear response range, the sensitivity and the detection limit for glucose detection of the sensor prepared in this work were much better.

3.5. Selectivity, stability, repeatability and reproducibility

The effect of the pH of the electrolyte solution on glucose detection was investigated. Figure 6(A) shows a plot of the amperometric responses of the sensor versus different pHs in 0.05 M PBS +0.1 M KCl (5.0–7.4) in the presence of 0.2 mM glucose. The sensor showed the best electrocatalytic activity in an electrolyte solution of pH 6.0. The effect of the temperature of the electrolyte solution on glucose detection was also investigated. Figure 6(B) shows a plot of the amperometric responses of the sensor versus different temperatures in 0.05 M PBS + 0.1 M KCl (20–55 °C) in the presence of 0.2 mM glucose. The sensor showed the best electrocatalytic activity at 45 °C. Human serum samples were made up of many substances, thus interference is inevitable in the determination of glucose. Chemicals such as uric acid, ascorbic acid, dopamine, mannose, galactose, fructose, lactate, bovine serum albumin and L-cysteine in a five-fold concentration and common ions such as Na^+, Ca^{2+} and Mg^{2+} in a five-fold concentration did not show interference to glucose detection (figure 6(C)). The stability of the sensor was also investigated. The current response kept 95% of the original current for 0.5 mM glucose for 35 min (figure 6(D)). The maximum time that the sensor could be operated at a given potential without significant deterioration was about 30 min. After the sensor was stored in an inverted beaker at 4 °C for 30 days, the current response to 1.0 mM glucose only decreased by 3.1% from the original value. The repeatability of the current response of one sensor to five successive amperometric measurements of 1.0 mM glucose was checked. A relative standard deviation (RSD) value of 5.6% was calculated for the steady current density. The electrode-to-electrode reproducibility was determined from the response to 1.0 mM glucose at five different sensors. They yielded a RSD of 6.4%.

4. Conclusions

In summary, a novel PB–FCNF nanocomposite was successfully prepared by a facile method. The electrochemical and electrocatalytic behaviors of the PB–FCNF nanocomposites obtained at different reaction times were investigated. Our experiments confirmed that when the reaction time was 144 h, the resulting PB–FCNF nanocomposite-modified electrode showed the maximal electrocatalytic ability for the reduction of H_2O_2. Furthermore, a glucose biosensor was successfully constructed based on a PB–FCNF/GCE. Mass production of PAN nanofibers is being carried out in our group for application in a battery separator. Accordingly, the synthesis

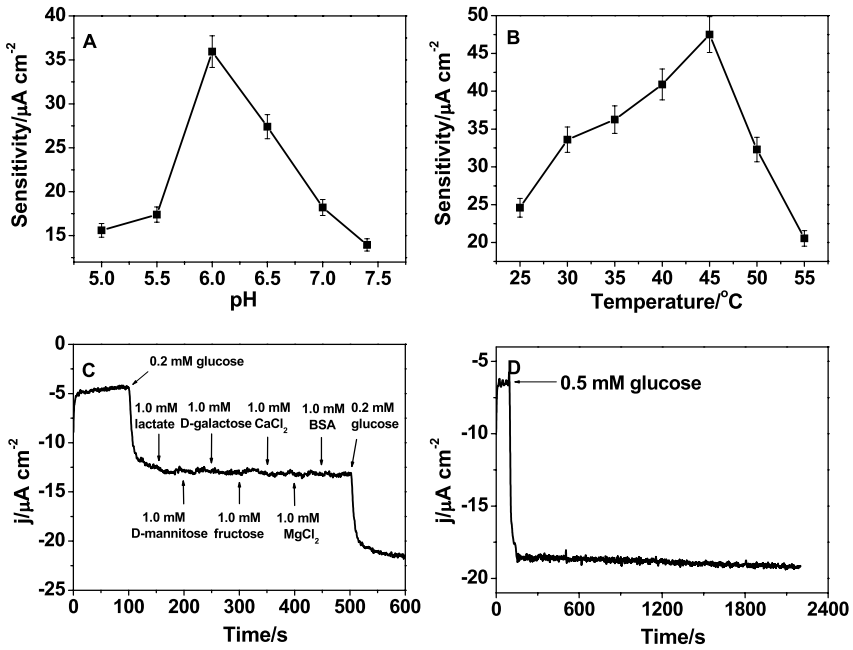

Figure 6. ((A), (B)) Effects of pH (A) and temperature (B) of 0.05 M PBS+0.1 M KCl on glucose detection at the GOD/PB–FCNF/GCE. (C) The interference effect of some electro-active substance on glucose detection at the GOD/PB–FCNF/GCE. (D) The recorded chronoamperogram over a long time period. Applied potential: 0.12 V.

of PB–FCNF nanocomposites should be compatible with mass production. Compared to commercial glucose sensors, the glucose sensor based on PB–FCNF nanocomposites is of low cost and shows good stability and selectivity. Therefore, the proposed biosensor might be effectively applied for glucose measurements.

Acknowledgments

This work was financially supported by National Natural Science Foundation of China (20905032, 21065005, 21165010), Young Scientist Foundation of Jiangxi Province (20112BCB23006), Foundation of Jiangxi Educational Committee (GJJ10389), the State Key Laboratory of Electroanalytical Chemistry (2008003) and the Scientific Research Foundation for the Returned Overseas Chinese Scholars, State Education Ministry.

References

[1] Zhang Y, Su L, Manuzzi D, de los Monteros H V, Jia W, Huo D, Hou C and Lei Y 2012 Ultrasensitive and selective non-enzymatic glucose detection using copper nanowires *Biosens. Bioelectron.* **31** 426–32

[2] Yang J, Jiang L C, Zhang W D and Gunasekaran S 2010 A highly sensitive non-enzymatic glucose sensor based on a simple two-step electrodeposition of cupric oxide (CuO) nanoparticles onto multi-walled carbon nanotube arrays *Talanta* **82** 25–33

[3] Yehezkeli O, Tel-Vered R, Reichlin S and Willner I 2011 Nano-engineered flavin-dependent glucose dehydrogenase/gold nanoparticle-modified electrodes for glucose sensing and biofuel cell applications *ACS Nano* **5** 2385–91

[4] Jin L H, Shang L, Guo S J, Fang Y X, Wen D, Wang L, Yin J Y and Dong S J 2011 Biomolecule-stabilized Au nanoclusters as a fluorescence probe for sensitive detection of glucose *Biosens. Bioelectron.* **26** 1965–9

[5] Yan Y M, Tel-Vered R, Yehezkeli O, Cheglakov Z and Willner I 2008 Biocatalytic growth of Au nanoparticles immobilized on glucose oxidase enhances the ferrocene-mediated bioelectrocatalytic oxidation of glucose *Adv. Mater.* **20** 2365–70

[6] Zheng M, Cui Y, Li X Y, Liu S Q and Tang Z Y 2011 Photoelectrochemical sensing of glucose based on quantum dot and enzyme nanocomposites *J. Electroanal. Chem.* **656** 167–73

[7] Luo S, Su F, Liu C, Li J, Liu R, Xiao Y, Li Y, Liu X and Cai Q 2011 A new method for fabricating a CuO/TiO_2 nanotube arrays electrode and its application as a sensitive nonenzymatic glucose sensor *Talanta* **85** 157–63

[8] Wang S M, Su P, E H J and Yang Y 2010 Polyamidoamine dendrimer as a spacer for the immobilization of glucose oxidase in capillary enzyme microreactor *Anal. Biochem.* **405** 230–5

[9] Pleitez M, von Lilienfeld-Toal H and Mantelea W 2012 Infrared spectroscopic analysis of human interstitial fluid *in vitro* and *in vivo* using FT-IR spectroscopy and pulsed quantum cascade lasers (QCL): establishing a new approach to non invasive glucose measurement *Spectrochim. Acta* A **85** 61–5

[10] Bahshi L, Freeman R, Gill R and Willner I 2009 Optical detection of glucose by means of metal nanoparticles (NPs) or semiconductor quantum dots *Small* **5** 676–80

[11] Li X Y, Zhou Y L, Zheng Z Z, Yue X L, Dai Z F, Liu S Q and Tang Z Y 2009 Glucose biosensor based on nanocomposite films of CdTe quantum dots and glucose oxidase *Langmuir* **25** 6580–6

[12] Wu W T, Chen S M, Hu Y M and Zhou S Q 2012 A fluorescent responsive hybrid nanogel for closed-loop control of glucose *J. Diabetes Sci. Technol.* **6** 892–901

[13] Wu W T, Zhou T, Aiello M and Zhou S Q 2010 Construction of optical glucose nanobiosensor with high sensitivity and selectivity at physiological pH on the basis of organic–inorganic hybrid microgels *Biosens. Bioelectron.* **25** 2603–10

[14] Wu W T, Shen J, Li Y X, Zhu H B, Baneriee P and Zhou S Q 2012 Specific glucose-to-SPR signal transduction at physiological pH by molecularly imprinted responsive hybrid microgels *Biomaterials* **33** 7115–25

[15] Yan Y M, Baravik I, Yehezkeli O and Willner I 2008 Integrated electrically contacted glucose oxidase/carbon nanotube electrodes for the bioelectrocatalyzed detection of glucose *J. Phys. Chem.* C **112** 17883–8

[16] Li X, Zhu Q, Tong S, Wang W and Song W 2009 Self-assembled microstructure of carbon nanotubes for enzymeless glucose sensor *Sensors Actuators* B **136** 444–50

[17] Wang Y, Liu L, Li M, Xu S and Gao F 2011 Multifunctional carbon nanotubes for direct electrochemistry of glucose oxidase and glucose bioassay *Biosens. Bioelectron.* **30** 107–11

[18] Satheesh Babu T G and Ramachandran T 2010 Development of highly sensitive non-enzymatic sensor for the selective determination of glucose and fabrication of a working model *Electrochim. Acta* **55** 1612–8

[19] Luo J, Jiang S, Zhang H, Jiang J and Liu X 2012 A novel non-enzymatic glucose sensor based on Cu nanoparticle modified graphene sheets electrode *Anal. Chim. Acta* **709** 47–53

[20] Yang J, Zhang W and Gunasekaran S 2010 An amperometric non-enzymatic glucose sensor by electrodepositing copper nanocubes onto vertically well-aligned multi-walled carbon nanotube arrays *Biosens. Bioelectron.* **26** 279–84

[21] Chen J, Zhang W and Ye J 2008 Nonenzymatic electrochemical glucose sensor based on MnO_2/MWNTs nanocomposite *Electrochem. Commun.* **10** 1268–71

[22] Mu Y, Jia D, He Y, Miao Y and Wu H 2011 Nano nickel oxide modified non-enzymatic glucose sensors with enhanced sensitivity through an electrochemical process strategy at high potential *Biosens. Bioelectron.* **26** 2948–52

[23] Lu L, Zhang L, Qu F, Lu H, Zhang X, Wu Z, Huan S, Wang Q, Shen G and Yu R 2009 A nano-Ni based ultrasensitive nonenzymatic electrochemical sensor for glucose: enhancing sensitivity through a nanowire array strategy *Biosens. Bioelectron.* **25** 218–23

[24] Haghighi B, Hamidi H and Gorton L 2010 Electrochemical behavior and application of Prussian blue nanoparticle modified graphite electrode *Sensors Actuators* B **147** 270–6

[25] Zhang Y, Sun X, Zhu L, Shen H and Jia N 2011 Electrochemical sensing based on graphene oxide/Prussian blue hybrid film modified electrode *Electrochim. Acta* **56** 1239–45

[26] García-Jareño J J, Navarro-Laboulais J and Vicente F 1996 Electrochemical study of nafion membranes/Prussian blue films on ITO electrodes *Electrochim. Acta* **41** 2675–82

[27] Liu X W, Yao Z J, Wang Y F and Wei X W 2010 Graphene oxide sheet-Prussian blue nanocomposites: green synthesis and their extraordinary electrochemical properties *Colloids Surf.* B **81** 508–12

[28] Jin E, Lu X F, Cui L L, Chao D M and Wang C 2010 Fabrication of graphene/Prussian blue composite nanosheets and their electrocatalytic reduction of H_2O_2 *Electrochim. Acta* **55** 7230–4

[29] Zhang W, Wang L L, Zhang N, Wang G and Fang B 2009 Functionalization of single-walled carbon nanotubes with cubic Prussian blue and its application for amperometric sensing *Electroanalytical* **21** 2325–30

[30] Zhai J F, Zhai Y M, Wen D and Dong S J 2009 Prussian blue/multiwalled carbon nanotube hybrids: synthesis, assembly and electrochemical behavior *Electroanalysis* **21** 2207–12

[31] Cui K, Song Y, Guo Q, Xu F, Zhang Y, Shi Y, Wang L, Hou H and Li Z 2011 Architecture of electrospun carbon nanofibers–hydroxyapatite composite and its application act as a platform in biosensing *Sensors Actuators* B **160** 435–40

[32] Huang J S, Liu Y, Hou H Q and You T Y 2008 Simultaneous electrochemical determination of dopamine, uric acid and ascorbic acid using palladium nanoparticle-loaded carbon nanofibers modified electrode *Biosens. Bioelectron.* **24** 632–7

[33] Liu Y, Teng H, Hou H Q and You T Y 2009 Nonenzymatic glucose sensor based on renewable electrospun Ni nanoparticle-loaded carbon nanofiber paste electrode *Biosens. Bioelectron.* **24** 3329–34

[34] Song Y H, He Z F, Xu F G, Hou H Q and Wang L 2012 pH-controlled electrocatalysis of amino acid based on electrospun cobalt nanoparticles-loaded carbon nanofibers *Sensors Actuators* B **166/167** 357–64

[35] Huang J S, Hou H Q and You T Y 2009 Electrochemical detection of hydrazine based on electrospun palladium nanoparticle/carbon nanofibers *Electrochem. Commun.* **11** 1281–4

[36] Hou H Q and Reneker D H 2004 Carbon nanotubes on carbon nanofibers: a novel structure based on electrospun polymer nanofibers *Adv. Mater.* **16** 69–73

[37] Cao L, Liu Y, Zhang B and Lu L 2010 *In situ* controllable growth of Prussian blue nanocubes on reduced graphene oxide: facile synthesis and their application as enhanced nanoelectrocatalyst for H_2O_2 reduction *ACS Appl. Mater. Interfaces* **2** 2339–46

[38] Zhang Z P and Han M Y 2003 Synthesis of carbon nanotubes by pyrolysis of acetylene using alloy hydride materials as catalysts and their hydrogen adsorption studies *Chem. Phys. Lett.* **374** 513–20

[39] Wei G, Zhou H L, Liu Z H, Song Y H, Wang L, Sun L P and Li Z 2005 One-step synthesis of silver nanoparticles, nanorods, and nanowires on the surface of DNA network *J. Phys. Chem.* B **109** 8738–43

[40] Wei Z, Mieszawska A J and Zamborini F P 2004 Synthesis and manipulation of high aspect ratio gold nanorods grown directly on surfaces *Langmuir* **20** 4322–6

[41] Wang X Y, Gu H F, Yin F and Tu Y F 2009 A glucose biosensor based on Prussian blue/chitosan hybrid film *Biosens. Bioelectron.* **24** 1527–30

[42] Chiu J Y, Yu C M, Yen M J and Chen L C 2009 Glucose sensing electrodes based on a poly(3,4-ethylenedioxythiophene)/Prussian blue bilayer and multi-walled carbon nanotubes *Biosens. Bioelectron.* **24** 2015–20

[43] Wang Z, Liu S N, Wu P and Cai C X 2009 Detection of glucose based on direct electron transfer reaction of glucose oxidase immobilized on highly ordered polyaniline nanotubes *Anal. Chem.* **81** 1638–45

[44] Li J, Wei X and Yuan Y 2009 Synthesis of magnetic nanoparticles composed by Prussian blue and glucose oxidase for preparing highly sensitive and selective glucose biosensor *Sensors Actuators* B **139** 400–6

[45] Zhong X, Yuan R and Chai Y Q 2012 Synthesis of chitosan-Prussian blue-graphene composite nanosheets for electrochemical detection of glucose based on pseudobienzyme channeling *Sensors Actuators* B **162** 334–40

[46] Li L, Sheng Q L, Zheng J B and Zhang H F 2008 Glucose biosensor based on the highly efficient immobilization of glucose oxidase on Prussian blue-gold nanocomposite films *Bioelectrochemistry* **74** 170–5